Received: 16 June 2024 | Revised: 19 August 2024 | Accepted: 24 September 2024

DOI: 10.1002/cey2.673

RESEARCH ARTICLE

CARBON ENERGY WILEY

# Template-oriented synthesis of boron/nitrogen-rich carbon nanoflake superstructure for high-performance Zn-ion hybrid capacitors

**Chunjiang Jin**[1] | **Fengjiao Guo**[1] | **Hongyu Mi**[1] | **Nianjun Yang**[2] | **Congcong Yang**[1] | **Xiaqing Chang**[1] | **Jieshan Qiu**[3]

[1]School of Chemical Engineering and Technology, Xinjiang University, Urumqi, China

[2]Department of Chemistry and IMOIMEC, Hasselt University, Diepenbeek, Belgium

[3]State Key Laboratory of Chemical Resource Engineering, College of Chemical Engineering, Beijing University of Chemical Technology, Beijing, China

**Correspondence**
Hongyu Mi and Xiaqing Chang, School of Chemical Engineering and Technology, Xinjiang University, Urumqi 830017, China.
Email: mmihongyu@xju.edu.cn and cxq2018400097@163.com

Jieshan Qiu, State Key Laboratory of Chemical Resource Engineering, College of Chemical Engineering, Beijing University of Chemical Technology, Beijing 100029, China.
Email: qiujs@mail.buct.edu.cn

**Funding information**
Natural Science Foundation of Xinjiang Uygur Autonomous Region, Grant/Award Number: 2023D01C11; National Natural Science Foundation of China, Grant/Award Numbers: 22369019, U2003216; Special Projects on Regional Collaborative Innovation-SCO Science and Technology Partnership Program, International Science and Technology Cooperation Program, Grant/Award Number: 2022E01020; Tianshan Talent Training Program, Grant/Award Number: 2023TSYCLJ0019; National Key Research and Development Program of China, Grant/Award Numbers: 2022YFB4101600, 2022YFB4101601

## Abstract

The rise of Zn-ion hybrid capacitor (ZHC) has imposed high requirements on carbon cathodes, including reasonable configuration, high specific surface area, multiscale pores, and abundant defects. To achieve this objective, a template-oriented strategy coupled with multi-heteroatom modification is proposed to precisely synthesize a three-dimensional boron/nitrogen-rich carbon nanoflake-interconnected micro/nano superstructure, referred to as BNPC. The hierarchically porous framework of BNPC shares short channels for fast $Zn^{2+}$ transport, increased adsorption-site accessibility, and structural robustness. Additionally, the boron/nitrogen incorporation effect significantly augments $Zn^{2+}$ adsorption capability and more distinctive pseudocapacitive nature, notably enhancing Zn-ion storage and transmission kinetics by performing the dual-storage mechanism of the electric double-layer capacitance and Faradaic redox process in BNPC cathode. These merits contribute to a high capacity (143.7 mAh $g^{-1}$ at 0.2 A $g^{-1}$) and excellent rate capability (84.5 mAh $g^{-1}$ at 30 A $g^{-1}$) of BNPC-based aqueous ZHC, and the ZHC still shows an ultrahigh capacity of 108.5 mAh $g^{-1}$ even under a high BNPC mass loading of 12 mg $cm^{-2}$. More critically, the BNPC-based flexible device also sustains notable cyclability over 30,000 cycles and low-rate self-discharge of 2.13 mV $h^{-1}$ along with a preeminent energy output of 117.15 Wh $kg^{-1}$ at a power density of 163.15 W $kg^{-1}$, favoring a creditable applicability in modern electronics. In/ex-situ analysis and theoretical calculations elaborately elucidate the enhanced charge storage mechanism in depth. The findings offer a

promising platform for the development of advanced carbon cathodes and corresponding electrochemical devices.

**KEYWORDS**

active site density, carbon superstructure, heteroatom doping, MOF template, Zn-ion hybrid capacitor

## 1 | INTRODUCTION

Reaping the preponderances of source abundance, stable chemistry, non-toxicity, and appealing potential (−0.76 V vs. SHE) exhibited by metallic zinc, various Zn-ion batteries (ZIBs) have been widely developed as a new generation of low-cost and safe energy storage system (ESS). However, the power density of these batteries falls short of meeting the actual requirements, which prompts the exploration of strategies to maximize the power capability without significantly compromising the energy transmission. In light of this, sustainable aqueous zinc-based hybrid capacitors termed ZHCs with excellent environmental compatibility have emerged as a suitable choice in the near future, given their dual charge-storage feature involving adsorption/desorption (from the capacitive cathode) and Faradaic redox reactions (from battery-type zinc anode) that may potentially achieve high power/energy density.[1,2] Carbon materials, as the core component for energy storage, are being extensively pursued as electrodes for energy storage devices owing to their high electronic conductivity, environmental benignity, controllable structure, and stable electrochemistry. Commercial activated carbon (AC) with a high specific surface area (SSA) has attracted intensive attention as electrode material for electrical double-layer capacitors. However, AC has three apparent disadvantages, including the relatively unitary pore structure, moderate electrical conductivity, and poor wettability of electrolyte to AC's surface, which severely limit the Zn-ion storage performance of AC-based devices.[3] Our group investigated the electrochemical performance of ZHC fabricated with AC cathode (1600 $m^2 g^{-1}$, obtained from Kuraray Co.), Zn metal anode, and $ZnSO_4$ aqueous solution as electrolyte.[4] The device only exhibited a poor reversible capacity of 55.0 mAh $g^{-1}$ at 0.5 A $g^{-1}$ and 17.2 mAh $g^{-1}$ at 20 A $g^{-1}$. Thus, one of the pressing concerns in this domain lies in how to gain high-quality carbon cathodes for improving the ZHC performance.

It has been extensively demonstrated that the structural form of carbon materials has a profound impact on their electrochemical properties.[5,6] Among visible carbons in different dimensions,[7–10] the well-integrated carbon scaffolds fabricated from low-dimensional building blocks have provoked considerable attention, such as nanorod-integrated carbon superstructure and rationally designed two-dimensional (2D) nanosheet-assembled carbon superstructure,[11,12] given their ability to sustainably gather the physicochemical nature of building modules for achieving synergistic effects and offering stable frameworks and uninterrupted pathways for smooth mass/charge transmission.[13] Apart from the structural modulation, the development of rich porosity and a large surface area in carbon materials is crucial for facilitating the accessibility of active sites and accelerating the ion adsorption/desorption kinetics of ZHCs.[14] Nevertheless, the presence of excessively small pores can restrict the accessibility of electrolyte ions, leading to reduced utilization of the available surface area. This limitation has been demonstrated in previous studies, even for carbon cathodes with large surface areas and porous structures.[15–17] Consequently, the engineering of porous carbon (PC) materials with elaborately designed structures and desired pore sizes and distributions, as well as substantial accessible surface area, is absolutely pivotal in the quest for high-performance ZHCs.

In terms of the preparation of PC, compared with the traditional physical and chemical activation, the template strategy has garnered significant attention because of its ability to achieve precise regulation of the pore structure and morphology.[18] Notably, metal-organic frameworks (MOFs) are considered pioneering templates due to their well-arranged channels/pores and tunable structures/compositions, as well as the graphitization/activation effect imparted by the derived metals during pyrolysis.[19] Furthermore, the carbon materials prepared via the utilization of MOF templates can largely inherit the unique skeleton structures and high porosities of the precursor MOFs, which is conducive to enhancing the electrochemical properties. Various MOF templates, including Zn-MOF,[20] Ni-MOF,[21] and Co-MOF,[22] have already been explored for the fabrication of electrode materials exhibiting perfect cyclability and rate capability.

Despite considerable success in morphology and structure regulation, the mediocre capacitance/capacity problem caused by the typical adsorption/desorption storage principle for carbon materials has to be relieved toward practical applications. To further intensify the

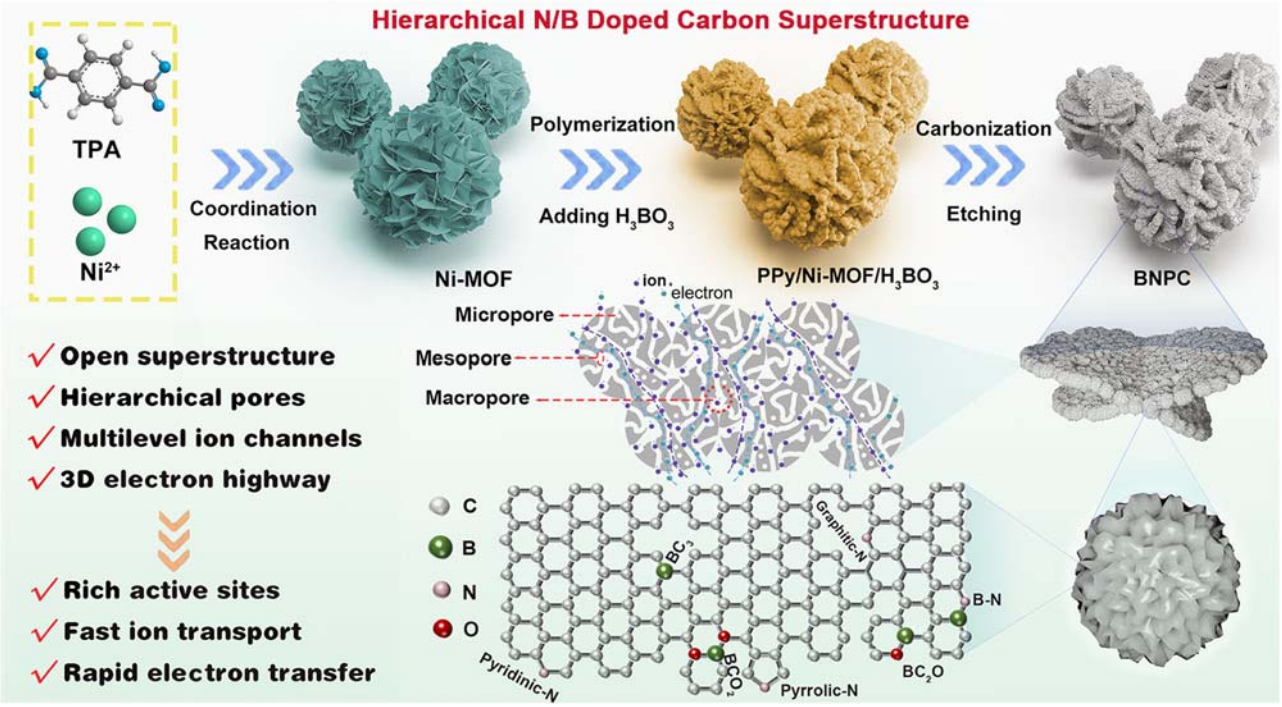


**FIGURE 1** Schematic illustration for the preparation and structure of the optimized BNPC.

capacitive characteristics, the heteroatom-modified strategy has been proposed.[23] As emphasized by Ostrikov et. al.,[24] heteroatom doping induces changes in the physicochemical properties of carbon materials due to the disparities in electronegativity and spin density between carbon (C) and dopant atoms (e.g., N, S, B, P). This modification not only enhances the electronic conductivity and promotes the electrolyte wettability but also offers appreciable pseudo-capacitance, collectively improving the capacitive properties of carbon materials. Heteroatom doping, especially multiple-heteroatom doping, could maintain the advantages of individual building units, offer considerable pseudo-capacity, and even create a new synergistic effect to boost the Zn-ion storage performance.[25] For instance, the N/O co-doped carbon superstructure contributed a large capacitance of 468 F $g^{-1}$ at 1 A $g^{-1}$ and demonstrated a high energy density of 128 Wh $kg^{-1}$.[26] Therefore, the reasonable structural engineering of carbon materials, accompanied by high multiple-atom doping, is highly promising for achieving high-efficiency ZHCs, whereas the construction of carbon materials with such desired properties still remains a challenge. Moreover, insights into the structure/composition-performance relationships are absolutely imperative for manufacturing advanced carbon cathodes.

Herein, we propose a 3D boron/nitrogen-rich carbon nanoflake-interconnected micro/nano superstructure (BNPC) with hierarchical porous architecture to explore high-performance ZHC cathode via the shape-preserving carbonization of PPy/Ni-MOF/$H_3BO_3$ with the assistance of polypyrrole (PPy) and boric acid ($H_3BO_3$), respectively, as nitrogen/carbon and boron sources. The resulting heteroatom-doped superstructure reaps the favorable traits of Ni-MOF, leading to the facile accessibility of active sites, exceptional structural integrity, and successive charge transfer channels. In addition, the B, N heteroatoms are available to improve the electronic conductivity, promote the wettability of carbon materials profiting from the acceleration of electrolyte permeation and diffusion, and provide numerous electrochemically active sites. These combined features synergistically contribute to the BNPC cathode's high specific capacity, unprecedented lifespan, and superior rate performance in the as-fabricated aqueous ZHCs. The mechanism of storage enhancement is further explored by in/ex-situ analysis and density functional theory (DFT) calculations.

## 2 | RESULTS AND DISCUSSION

### 2.1 | Preparation, morphology, and structure of BNPC

Figure 1 shows the schematic diagram illustrating the synthesis of BNPC, and it mainly involves three steps: (i) synthesis of Ni-MOF nanocrystals as the catalytic template via a hydrothermal coordinate reaction method; (ii)

in-situ polymerization of pyrrole (Py) and treatment with $H_3BO_3$ to obtain the PPy/Ni-MOF/$H_3BO_3$ precursor; (iii) pyrolysis of the precursor in an Ar flow and further etching to reap the BNPC product with the anticipative structure/component. As shown in Figure S1, Ni-MOF displays a flower-like morphology assembled by numerous interconnected nanoflakes with a thickness ranging from 10 to 50 nm, which could be ascribed to the mixed solvent of deionized (DI) water, ethanol, and dimethylformamide (DMF) that are used for hydrothermal process. The ethanol with the smallest polarity can increase the nucleation rate and induce the formation of nanoflakes, and DMF favors the framework construction of MOFs, while the DI water with the highest polarity can stabilize reactant ions and facilitate the generation of the flower-like structure, collectively providing a prerequisite for the fabrication of Ni-MOF with 3D hierarchical flower-like structure.[27,28] Subsequently, PPy uniformly in situ grew on the surface of Ni-MOF via the coordination interaction of the pyrrolic N atom with the Ni ion.[29] Notably, the introduction of PPy and followed $H_3BO_3$ treatment do make the PPy/Ni-MOF/$H_3BO_3$ precursor have a morphology change with nanoflakes covered by PPy and $H_3BO_3$ (Figure S2A), which can be further confirmed by X-ray diffraction (XRD) pattern and Fourier transform infrared (FTIR) spectroscopy analyses. The XRD pattern (Figure S2B) of Ni-MOF displays diffraction peaks belonging to Ni-based MOF as compared with reported work.[30] After PPy introduction, Ni-MOF/PPy shows similar diffraction peaks to Ni-MOF because of PPy's noncrystalline structure. Because of the strong peak intensity of the (002) plane of $H_3BO_3$, the addition of $H_3BO_3$ lead to significant changes in diffraction peaks, while the peaks corresponding to Ni-MOF/PPy remain unchanged. As shown in Figure S2C, the Ni-MOF/PPy/$H_3BO_3$ presents the characteristic bands of Ni-MOF (1581 $cm^{-1}$ of C=N band),[31] PPy (1562 and 1116 $cm^{-1}$ of C=C and C–N bands, respectively),[32] and additional bands representing B–O (1011 and 563 $cm^{-1}$) for $H_3BO_3$,[33] confirming the combination of Ni-MOF, PPy, and $H_3BO_3$ components.

Upon annealing treatment at 800°C, the PPy/Ni-MOF/$H_3BO_3$ precursor is transformed into BNPC. During which, the flower-shaped Ni-MOF holds a function in constructing a PC skeleton and PPy realizes active N introduction. Interestingly, $H_3BO_3$ can act more than the boron source for active B doping; meanwhile, it can also be utilized as an activator for a finer porous structure by releasing $H_2O$ (gas) during pyrolysis and removing $B_2O_3$ impurity in post-treatment. Based on the aforementioned understanding of the structural features of BNPC, Figure 1 also provides a concise summary of the advantages associated with the constructed B,N-rich carbon superstructure. First, the 3D flower-like BNPC with an open superstructure and developed micro/mesopores offers a substantial number of interfacial active sites and enhances ion diffusion by reducing the transport distance. Second, the presence of electron-rich N and electron-deficient B enables their conjugation into $\pi$ electron system, and these surface defects promote Faradaic reaction. Finally, the optimized surface wettability and electronic conductivity induced by B and N co-doping facilitate rapid charge transfer at the interfaces. These merits collectively contribute to the expectation of excellent electrochemical performance from the synthesized BNPC material.

Scanning electron microscopy (SEM), transmission electron microscopy (TEM), and high-resolution TEM (HRTEM) were used to examine the surface morphology and internal structure of the sample. The PC successfully replicates the geometric feature of its parent material (Ni-MOF) after high-temperature decomposition in an Ar flow (Figure S3A,B). The nitrogen doped porous carbon (NPC) also shows a well-preserved flower structure covered with numerous nanoparticles originating from the pyrolysis of PPy (Figure S3C,D). Comparatively, the PPy-derived nanoparticles could hardly be detected in the inherited micro-flower-shaped BNPC (Figure 2A), partially due to the activation effect of $H_3BO_3$. However, upon closer examination at higher magnification, it is clear that the BNPC is constituted with the interconnected nanoflakes (with an average thickness of 38 nm) mainly assembled from PPy-derived nanoparticles (Figure 2B–D), proving the successful fabrication of a unique porous superstructure for BNPC. Furthermore, the TEM image in Figure 2E discloses the presence of a multilevel porous structure within BNPC, and a disordered nanoarchitecture is visible by HRTEM and selected-area electron diffraction (SAED) images (Figure 2F and its inset). The amorphous structure of BNPC is further demonstrated by the XRD patterns with two broad and weak diffraction peaks at approximately 26.4° and 42.2° respectively ascribed to the (002) and (100) planes of graphite (Figure S4). Additionally, the elemental mapping images (Figure 2G) indicate a homogenous introduction of N, B, and O elements through BNPC. The heteroatoms in BNPC significantly facilitate electrolyte ion adsorption, as confirmed by the lowest contact angle of 25.8° in BNPC compared with 43.2° in PC and 37.3° in NPC (Figure S5). X-ray photoelectron spectroscopy (XPS) characterization was carried out to determine the chemical composition of samples. Figure S6 presents the XPS spectra of PC, NPC, and BNPC, revealing signals attributed to the C 1s, N 1s, and O 1s at specific binding energies of 284.8, 400.1, and 530.3 eV, respectively. Notably, the BNPC spectrum

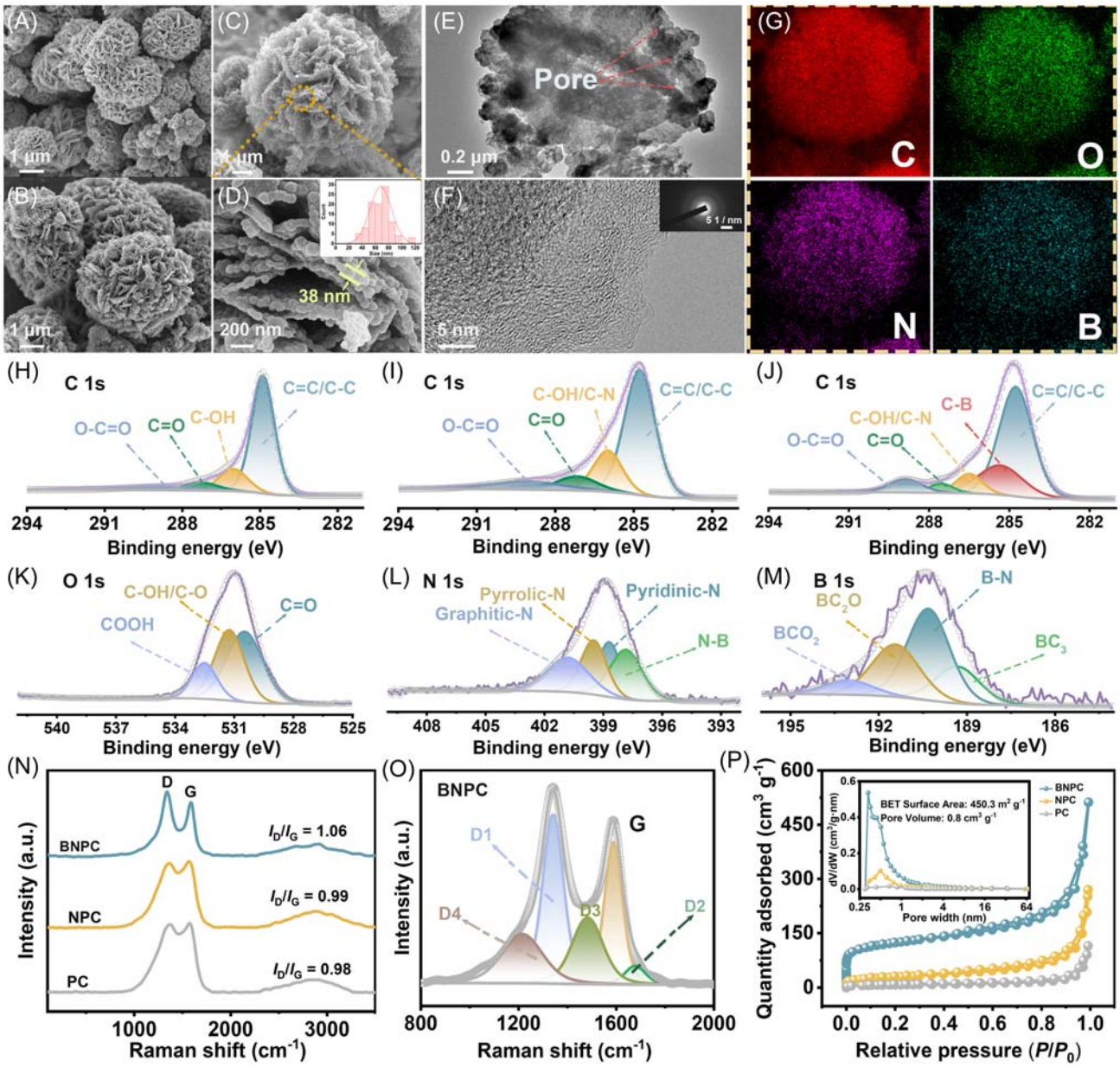


**FIGURE 2** (A–D) SEM images of BNPC with different magnifications. (E) TEM images of BNPC. (F) HRTEM image of BNPC with the SAED image (inset). (G) Corresponding elemental mapping results of BNPC. (H–J) C 1s XPS spectra of PC, NPC, and BNPC. (K–M) O 1s, N 1s, and B 1s XPS spectra of BNPC. (N) Raman spectra of BNPC, NC, and PC. (O) Deconvoluted Raman spectra of BNPC. (P) Nitrogen adsorption-desorption isotherms with pore size distribution plots for BNPC, NC, and PC.

exhibits an additional peak at 191.0 eV corresponding to B 1s, indicating the co-doping of B and N in BNPC. The doping atom contents of N and B in BNPC are 6.6 and 4.0 at%, respectively, whose N content surpasses those of 6.4 and 1.1 at% in NPC and PC samples (Figure S7). This disparity in N content could be due to the mutual promotion of B, N co-doping during the pyrolysis process, as the introduction of electron-accepting B atoms effectively increases the electron-deficient holes surrounding the nearby C atoms, thus boosting the further combination of C atoms with electron-donating N atoms.[22,34] The high-resolution C 1s spectra of PC and NPC (Figure 2H,I) are deconvoluted into four distinct peaks at approximately 284.8, 286.0, 287.2, and 289.2 eV, correlating with C=C/C–C, C–OH/C–N, C=O, and O–C=O, respectively.[35] Compared with PC and NPC, the additional peak associated with C–B (285.2 eV) appears in the high-resolution C 1s spectrum of BNPC (Figure 2J), indicating the realization of N, B co-doping via the formation of C–N and C–B bonds.[36] The high-resolution O 1s spectrum for the BNPC sample can be resolved to three oxygen-based components,

corresponding to C=O (531.5 eV), C–O/C–OH (532.8 eV), and C–O–C (533.8 eV),[37] respectively (Figure 2K). Here, the introduction of abundant oxygen-containing functional groups into carbon can increase the surface wettability of the electrodes. In high-resolution N 1 s spectra of three samples (Figures 2L and S8), apart from the fitted peaks of graphitic-N (401.4 eV), pyrrolic-N (399.9 eV), and pyridinic-N (398.9 eV), BNPC displays an extra N–B bond at approximately 397.9 eV.[38] Notably, the substitution of carbon atoms on the edge by heteroatoms is of great importance in enhancing the adsorption of ions, as reported in K/Zn-ion storage.[39,40] Though BNPC has an N–B content of 28.1%, it still shows a higher total edge-nitrogen configuration content of 55.6% (pyrrolic-N of 24% and pyridinic-N of 31.6%) compared with that of 52.5% (pyrrolic-N of 29.2% and pyridinic-N of 23.3%) for PC (Figure S9). This improvement of edge-N configuration could originate from the selective conversion of graphitic N into pyrrolic N in the carbon skeleton after the introduction of B atoms.[41,42] Figure 2M presents the high-resolution B 1s spectrum of BNPC with four deconvoluted peaks, including $BC_3$ (189.7 eV), B–N (191.3 eV), $BC_2O$ (192.3 eV), and $BCO_2$ (193.1 eV), which is favorable for the further facilitation of surface redox reactions in the appearance of N due to the heteroatoms co-doping induced synergistic effect and decreased band gap.[43,44] Furthermore, probably as the similar atomic diameters of B, C, and N result in negligible changes in dipole moment, the FTIR spectroscopy of BNPC in Figure S10 solely exhibits bands at 1568 $cm^{-1}$ (C=C) and 1258 $cm^{-1}$ (C–O), with no visible bands relating to C=N, C–N, B–C, and B–N.[45] Figure 2N presents the Raman spectroscopy of samples, which consists of a typical D band at 1350 $cm^{-1}$ relating to the disordered carbon and defects, and G band at 1580 $cm^{-1}$ representing the ordered graphite layers. The $I_D/I_G$ (the intensity ratio of D and G bands) value, which reflects the disorder degree of carbon material, increases from 0.98 for PC and 0.99 for NPC to 1.06 for BNPC, an indication of low graphitic degree and high defect density in BNPC.[46] Furthermore, a curve fitting in Gaussian-Lorentzian numerical simulation is adopted to subdivide the D band into the D1, D2, D3, and D4 bands (Figure 2O).[47] As the D3 band at ~1500 $cm^{-1}$ corresponds to the defects derived from the organic molecules or functional groups, the higher $I_{D3}/I_G$ value of 0.82 for BNPC compared with 0.57 for PC and 0.64 for NPC (Figures 2O and S11) indicates that more B, N, and O groups exist in carbon structure, which benefits to enhancing the electronic conductivity and electrolyte wettability of carbon materials. More importantly, the C–OH and C=O oxygen-containing groups can introduce additional pseudo-capacitance,[48] and B, N heteroatoms can efficiently modulate the electron-donor properties of neighboring C atoms and create charge sites, boosting Zn-ion storage performance.[49] Nitrogen absorption-desorption measurement was carried out to unveil the pore structure of BNPC. As shown in Figure 2P, the BNPC sample presents a typical type-IV isotherm with a sharp uptake at low relative pressure of $P/P_0 < 0.05$, a hysteresis loop at high relative pressure of $P/P_0$ in a range of 0.4–0.95, and a significant rise at $P/P_0 > 0.95$, revealing a hierarchical structure with micro-meso-macropores. Besides, BNPC has a wider micropore size distribution primarily located between 0.3 and 0.6 nm, which is quite distinct from that of PC and NPC with micropore size mainly centered at 0.3 and 0.5 nm, respectively (the inset of Figure 2P). The SSA of BNPC, NPC, and PC are determined to be 450.3, 102.1, and 27.3 $m^2 g^{-1}$, and their corresponding total volumes are 0.8, 0.4, and 0.2 $cm^3 g^{-1}$, respectively, as listed in Table S1. The larger SSA of BNPC compared to NPC and PC could be attributed to the porosity modulation of $H_3BO_3$ during pyrolysis. These findings have significant implications for available Zn-ion storage and rapid adsorption/desorption processes of hydrated Zn ions in BNPC. Consequently, the improved Zn-ion storage capacity and rate performance of BNPC-assembled devices can be anticipated.

## 2.2 | Electrochemical evaluation

The electrochemical properties of samples were evaluated by assembling an aqueous ZHC with a CR2023-type coin cell. As shown in Figure 3A, the cyclic voltammetry (CV) profiles of Zn//PC and Zn//NPC ZHCs exhibit near-rectangular shapes within the voltage range of 0.2–1.8 V. Whereas, the CV profile of the Zn//BNPC ZHC deviates from the ideal rectangle with an obvious pair of Faradaic charge/discharge redox humps at 0.8/1.1 V, which could be attributed to the conversion between C=O and C–OH.[50,51] That is, C=O could react with $H^+$ to transform into C–OH at 0.8 V in the discharge process, while the reversible reaction occurs as the charge process deepens to 1.1 V. Impressively, due to the structure superiority and synergistic effect of simultaneously induced O, B, N dopants on pseudo-capacitance, the CV profile of BNPC-based ZHC shows much-enhanced peak intensity and a larger area with the Zn//NPC and Zn//PC ZHCs as references, manifesting the largest Zn-ion storage capacity of Zn//BNPC ZHC. The galvanostatic charge-discharge (GCD) curves at 0.2 A $g^{-1}$ in Figure S12 further confirm the outstanding electrochemical performance of the Zn//BNPC ZHC, which delivers the highest specific capacity of 143.7 mAh $g^{-1}$ compared with 102.5 and 55.7 mAh $g^{-1}$ of Zn//NPC and Zn//PC ZHCs, respectively.

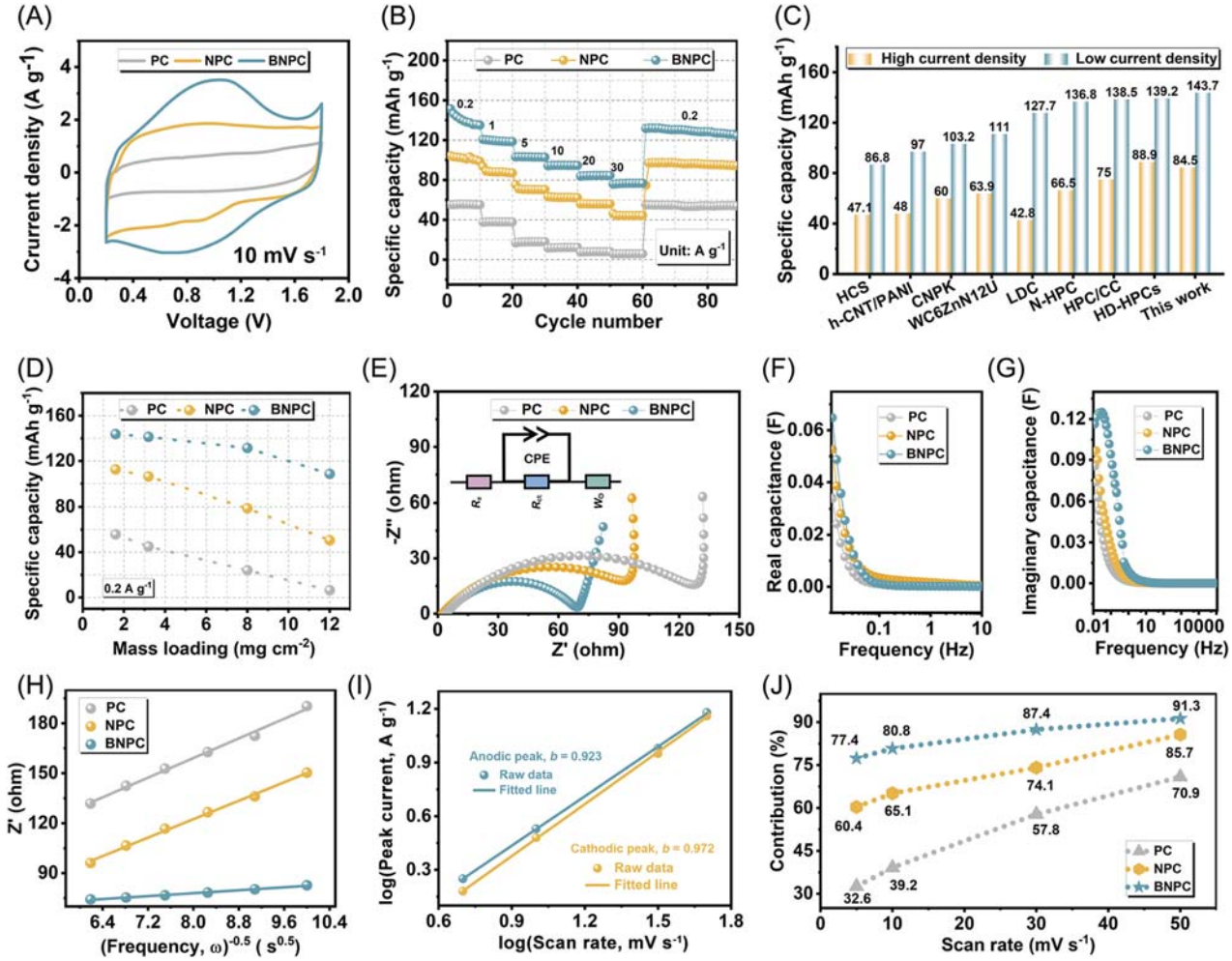


**FIGURE 3** (A) CV profiles and (B) rate performance of Zn//PC, Zn//NPC, and Zn//BNPC ZHCs. (C) Comparison of rate capability between the Zn//BNPC ZHC and the previously reported heteroatom-doped porous carbon-based ZHCs. (D) Specific capacities at 0.2 A $g^{-1}$ for Zn//PC, Zn//NPC, and Zn//BNPC ZHCs with different mass loadings. (E) EIS spectra with an inserted simulating equivalent circuit. (F) Real capacitance and (G) imaginary capacitance versus frequency. (H) The $Z'$–$\omega^{-1/2}$ plots for Zn//PC, Zn//NPC, and Zn//BNPC ZHCs. (I) Relationship between scan rate and peak current of the Zn//BNPC ZHC. (J) Capacitive contribution ratios of Zn//PC, Zn//NPC, and Zn//BNPC ZHCs at 3–50 mV $s^{-1}$.

Figure 3B shows the rate performance of aqueous Zn//BNPC ZHC in reference to Zn//PC ZHC and Zn//NPC ZHC. Different from the Zn//PC ZHC, which only maintains a capacity of 5.9 mAh $g^{-1}$ at a current density of 30 A $g^{-1}$, the Zn//NPC ZHC exhibits relatively superior performance with a capacity of 44.4 mAh $g^{-1}$ as the current density increases to 30 A $g^{-1}$. In contrast, the Zn//BNPC ZHC demonstrates an exceptional rate performance, achieving capacities of 84.5 mAh $g^{-1}$ at 30 A $g^{-1}$. Moreover, Figure 3C provides an intuitive comparison of the Zn-ion storage performance among different devices. It clearly illustrates that the Zn//BNPC ZHC exhibits significantly superior rate capability and surpasses many previously reported devices with heteroatom-doped porous carbon cathodes.[1,4,7–9,52–54] To further assess the performance of three cathodes in practical application, the capacities of the Zn//PC, Zn//NPC, and Zn//BNPC ZHCs were checked under various mass loadings at a current density of 0.2 A $g^{-1}$, as displayed in Figure 3D. Remarkably, the Zn//BNPC ZHC exhibits an exceptional capacity of 108.5 mAh $g^{-1}$ even under a high mass loading of 12 mg $cm^{-2}$, which is much higher than 50.5 mAh $g^{-1}$ of Zn//NPC ZHC and 6.4 mAh $g^{-1}$ of Zn//PC ZHC, an indication of great application prospects for real-world applications.

To comprehend the superior Zn-ion rate capability of the BNPC-based ZHC, electrochemical impedance spectroscopy (EIS) was conducted to study the electron/ion transport behavior.[55] As shown in Figure 3E, the charge transfer resistance ($R_{ct}$) associated with the apparent semicircle in the Nyquist plot is deduced based on the equivalent circuit. The BNPC-based ZHC displays a

lower $R_{ct}$ value of 65.2 Ω in reference to those of the NPC-based ZHC (80.4 Ω) and PC-based ZHC (135.7 Ω), primarily attributed to the enhanced electronic conductivity promoted by heteroatom doping. Furthermore, a common complex model of the capacitance was used to measure capacitance variations across a wide frequency range, employing the following Equation (1). Notably, the $C''(\omega)$ (imaginary capacitance) and $C'(\omega)$ (real capacitance) versus the frequency were derived from EIS data.

$$C(\omega) = C'(\omega) + jC''(\omega). \quad (1)$$

As seen in Figure 3F, the BNPC-based ZHC represents the highest real capacitance value of 64.9 mF compared to the NPC-based ZHC (52.6 mF) and PC-based ZHC (33.0 mF), further proving its excellent capacitive capability. To reflect the length of time that is required to deliver the stored energy and power efficiently, the relaxation time constant $\tau_0$ was calculated based on the equation of $\tau_0 = 1/f$ ($f$ represents the peak value of $C''$). From Figure 3G, the BNPC-based ZHC demonstrates a smaller $\tau_0$ value of 33.3 s than 71.4 s for NPC-based ZHC and 83.3 s for PC-based ZHC, implying the lower energy loss and faster electrolyte ion transportation in BNPC. The faster Zn-ion diffusion coefficient in the BNPC is further confirmed by the Warburg factor ($\sigma_\omega$), which is inversely proportional to the ion diffusion coefficient and can be calculated via the linear fitting of $Z'$ and $\omega^{-1/2}$ (Figure 3H).[56] The $\sigma_\omega$ values of PC-based ZHC and NPC-based ZHC are 14.7 and 13.9 Ω $S^{-1/2}$, respectively, while the optimized porous superstructure of NBPC endows the NBPC-based ZHC with a smaller $\sigma_\omega$ value of 2.2 Ω $S^{-1/2}$, an indication of the rapid charge/discharge process for Zn-ion storage and thus a good rate performance.[57]

CV measurements were performed at a wide range of scan rates from 5 to 50 mV $s^{-1}$ to explore the electrochemical reaction mechanism of the BNPC-based ZHC, as depicted in Figure S13A. The relationship between the scan rate ($v$) and the peak current ($i$) can be revealed by the equation $i = av^b$, and the exponent $b$ acquired by linear fitting of log($i$) and log($v$) is adopted to evaluate the electrochemical mechanism. The BNPC-based ZHC with a notably high $b$ value of almost 1.0 (0.923 and 0.972 for anodic and cathodic peaks, respectively) in Figure 3I strongly implies a capacitive dominant controlled behavior. Furthermore, the quantitative contributions of the capacitive-controlled and diffusion-controlled behaviors are determined via the equation $i(V) = k_1 v + k_2 v^{1/2}$. Figure S13B shows that the percentage of the capacitive contribution for the BNPC-based ZHC is up to 80.8% at 10 mV $s^{-1}$. As the scan rate escalates, the capacitive contribution experiences gradual enhancement, culminating in a maximum percentage of 91.3% at 50 mV $s^{-1}$ (Figure 3J). The capacitive contribution encompassing the electric double-layer capacitance and the surface Faradic pseudocapacitance can provide efficient charge transfer.[58] Therefore, the BNPC-based ZHC, characterized by its dominance of capacitive contribution, can easily store and deliver energy.

More encouraging is that the Zn//BNPC ZHC demonstrates remarkable cycle durability, as evidenced by a higher capacity retention of up to 92.7% in reference with Zn//PC ZHC (73.8%) and Zn//NPC ZHC (85.5%) after 10,000 cycles at 5 A $g^{-1}$ (Figure 4A). The morphology of cycled BNPC in Figure S14 with an integral carbon superstructure after long-term cycling suggests its structural firmness in ZHC. Additionally, Figure S15 displays the digital photos of post-cycling assembled coin-type Zn//BNPC ZHC to visually investigate the appearance change after cycling. As seen, no noticeable cracks can be observed in Zn//BNPC ZHC after cycling, further underscoring the structural stability of the assembled ZHC. Even when the current density increases to 10 A $g^{-1}$, the Zn//BNPC ZHC still shows an ultrahigh capacity retention of 98.7% over 30,000 cycles (Figure 4B). The post-cycling investigation was then carried out to evaluate the structural durability of BNPC. The cycled BNPC basically maintains its initial flower shape (insets of Figure 4B), corroborating the structural tolerance of the BNPC electrode and the outstanding cycle performance of the Zn//BNPC ZHC. As shown in Figures S16 and S17, the elemental percentages of BNPC electrodes before and after cycling were determined by XPS characterization to confirm the chemical stability of carbon material. The elemental contents of B, N, and O after cycling are 3.55, 6.25, and 11.54 at%, respectively, which display a slight change from 3.78, 6.45, and 11.23 at% before cycling, implying the stable structure of BNPC. Besides, the anti-self-discharge capability, which is often overlooked and is an important parameter for practical applications, can be assessed by monitoring the open-circuit voltage (OCV) change of the fully charged ZHC. In our study, the open-circuit voltage of the ZHC device was recorded as a function of time after the cell was charged to 1.8 V at 0.2 A $g^{-1}$ (inset of Figure 4C). The OCV drops to 1.16 V after 300 h, corresponding to a self-discharge rate of 2.13 mV $h^{-1}$, which is lower than that of many other capacitor devices (Figure 4C).[4,40,59–64] More impressively, the Zn//BNPC ZHC delivers a large energy density of 117.15 Wh $kg^{-1}$ at a power density of 163.15 W $kg^{-1}$ (based on the mass of the prepared carbon material) and a maximal power density of 21.6 kW $kg^{-1}$ at an energy density of 54.0 Wh $kg^{-1}$, surpassing or at least comparable to the values from recently reported works

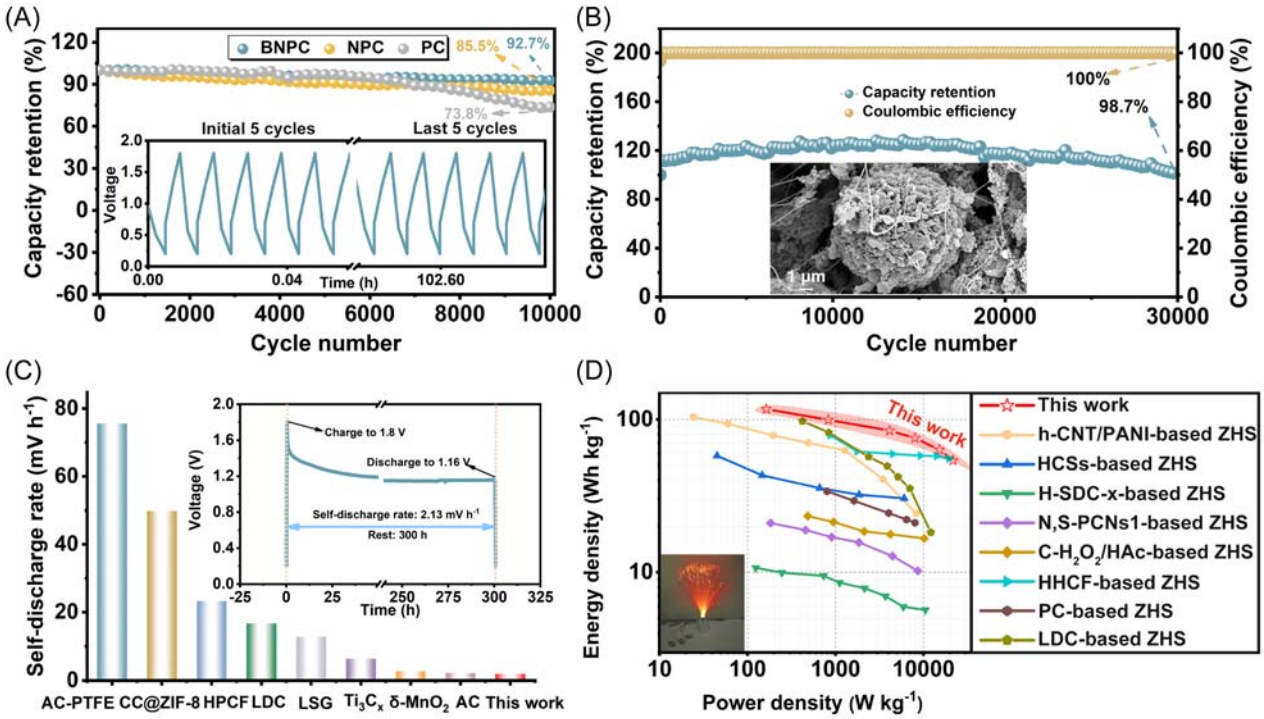


FIGURE 4 (A) Cycling performance of Zn//BNPC, Zn//NPC, and Zn//PC ZHCs at 5 A $g^{-1}$ with inset showing galvanostatic charge/discharge profiles before and after cycling. (B) Long-term cycle stability of the as-assembled Zn//BNPC device at 10 A $g^{-1}$ for 30,000 cycles with post-cycling SEM images of the BNPC cathode in the inset. (C) Self-discharge rate comparison among Zn//BNPC ZHC and devices from reported works with the self-discharge profile of the Zn//BNPC ZHC in the inset. (D) Ragone plots of Zn//BNPC ZHC in reference to reported devices (inserted digital photo of LED lights).

(Figure 4D).[4,7,9,15–17,20,21] Meanwhile, the series connected to Zn//BNPC ZHC devices can supply energy for LED lights as shown in the inset of Figure 4D, confirming its potential practical application.

## 2.3 | Mechanism discussion

To explore the charge storage mechanism, ex-situ XRD and XPS characterizations were performed to analyze the structural and compositional changes of the BNPC cathode at specific charge/discharge states of a GCD profile presented in Figure 5A. The ex-situ XRD pattern of the BNPC cathode (Figure 5B) with strong diffraction peaks representing $Zn(CF_3SO_3)_2{\cdot}Zn(OH)_2$ at state III indicates that the formation/dissolution of $Zn(CF_3SO_3)_2{\cdot}Zn(OH)_2$ takes part in the BNPC cathode reactions besides the adsorption/desorption of electrolyte ions on the BNPC surfaces.[65] Specially, the formation of $Zn(CF_3SO_3)_2{\cdot}Zn(OH)_2$ is accompanied by the insertion of $H^+$ to guarantee a neutral charge environment.[66,67] The XRD results of the Zn anode in Figure 5C only present the diffraction peaks of Zn metal, which implies that the deposition/stripping of metallic Zn dominates the electrochemical reaction of the Zn anode. As seen from Figure S18, ex-situ XPS tests show that the intensity of Zn 2p increases from state I to state III, suggesting the rising content of $Zn^{2+}$. From state III to state V, the intensity of Zn 2p presents a decreasing tendency, a strong proof of the reversible adsorption/desorption of $Zn^{2+}$ on the BNPC surfaces. The intensity of S 2p (Figure 5D) is gradually enhanced and reaches its maximum at state III ascribing to the formation of $Zn(CF_3SO_3)_2{\cdot}Zn(OH)_2$. Then, it decreases from state III to state IV, while it becomes stronger at state V as the charging process deepens, proving that the $CF_3SO_3^-$ is further absorbed in the high-voltage range.[68] To elucidate the chemisorption process between Zn ions and oxygen functional groups, various charge/discharge states of high-resolution C 1s and O 1s XPS spectra were investigated. The C 1s spectra analysis (Figure 5E) reveals three primary peaks located at 287.6, 286.4, and 284.8 eV, corresponding to C–O–Zn, C–OH, and C=C/C–C groups, respectively. Notably, the intensity of C–OH gradually decreases during the discharging process from state I to state III, while it continuously increases with the charging process (state III to state V). Whereas, the C–O–Zn exhibits the strongest intensity at the fully discharged state (state III) and gradually weakens during charging. These results indicate the existence of reversible electrochemical reactions between C–OH and Zn ions. Moreover, the fitted O 1s spectrum

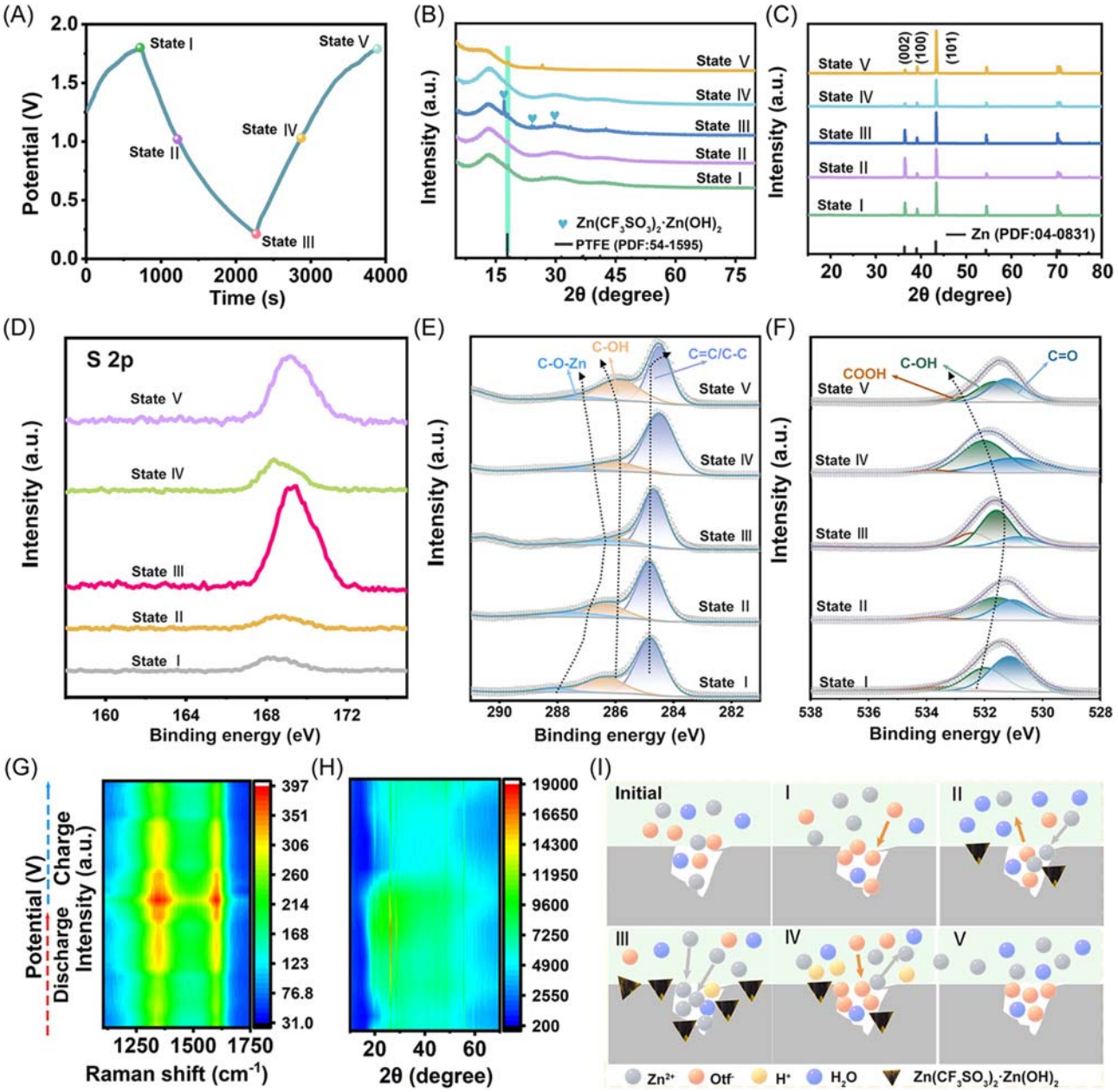


**FIGURE 5** Charge transfer behavior and storage kinetics of the Zn//BNPC ZHC. (A) The typical GCD curve of the Zn//BNPC ZHC at 0.2 A $g^{-1}$. Ex-situ XRD patterns of (B) BNPC cathode and (C) Zn anode at the selected states. Ex-situ (D) S 2p, (E) C 1s, and (F) O 1s XPS spectra of BNPC cathode. Contour-type in-situ electrochemical (G) Raman spectra and (H) XRD patterns of BNPC cathode. (I) Schematic illustration of the charge-storage mechanism for BNPC cathode in 1 M $Zn(CF_3SO_3)_2$ electrolyte.

(Figure 5F) shows a continuously decreased –C=O intensity during the discharging process, followed by increases upon the voltage returning back, opposite from the changing trend of –C – OH intensity, implying the reversible conversion between –C=O and –C–OH, which could promote the chemisorption of Zn ions during charge/discharge processes.

In-situ Raman technology was performed to observe the working process of the BNPC electrode in depth. As shown in Figure 5G, the intensities of the D and G bands gradually increase in discharging process and reach the strongest during deep discharging, and then progressively reduce during the subsequent charging. The enhanced defect degree of the BNPC electrode after the discharging process is ascribed to the co-adsorption of $Zn^{2+}/H^+$ on the carbon surface.[69] Impressively, the in-situ XRD measurement (Figure 5H) further demonstrates $H^+$ involvement during discharging process by observing the peak of $Zn(CF_3SO_3)_2{\cdot}Zn(OH)_2$ at 26.4°.[70] Based on the above ex-situ analysis and in-situ Raman and XRD techniques, the energy storage mechanism of the BNPC cathode could be

schematically illustrated in Figure 5I. Specifically, there is $Zn^{2+}$, $H^+$, and $CF_3SO_3^-$ co-adsorption during the charge storage process, and the $Zn^{2+}$ and $H^+$ adsorption/desorption mainly exists at low voltages, whereas the $CF_3SO_3^-$ adsorption/desorption mainly takes place at high voltages. It is worth noting that the adsorption/desorption of $H^+$ results in the reversible formation/dissolution of $Zn(CF_3SO_3)_2{\cdot}Zn(OH)_2$. Meanwhile, the invertible chemical adsorption of C−OH also occurs during the electrochemical process, providing enhanced capacitive performance. The possible reactions that happened on the BNPC cathode could be described as follows:

Physical adsorption/desorption:

$$C + Zn^{2+} + 2e^- \leftrightarrow C//Zn,$$
$$C//CF_3SO_3^- \leftrightarrow C + CF_3SO_3^-.$$

Chemical adsorption/desorption:

$$C{=}O + H^+ + e^- \leftrightarrow C{-}OH,$$
$$C{-}OH + Zn^{2+} + e^- \leftrightarrow C{-}O{-}Zn + H^+.$$

Precipitation/dissolution:

$$2Zn^{2+} + 4OH + 2Zn(CF_3SO_3)_2 + nH_2O \leftrightarrow 2\left[Zn(CF_3SO_3)_2 \cdot Zn(OH)_2\right] \cdot nH_2O.$$

DFT calculations were performed to investigate the function mechanism of graphitic N, pyrrolic N, pyridinic N, and B-N motifs on the $Zn^{2+}$ adsorption capability of BNPC cathode. Figure S19 displays the most stable states for $Zn^{2+}$ adsorption on graphene and graphitic-N, pyrrolic-N, pyridinic-N, pyrrolic-N-$BC_3$, pyrrolic-N-$BC_2O$, and pyrrolic-N-$BCO_2$ configurated graphene, and the corresponding adsorption energy is shown in Figure 6A. As seen, all the models show negative $\Delta E_a$ values, implying a positive effect on $Zn^{2+}$ adsorption. Among all these models, the pyrrolic-N-$BC_3$ configuration presents the strongest affinity and adsorption ability for $Zn^{2+}$ because of the smallest adsorption energy value of −0.190 eV. The correlation density of states is further calculated for a more in-depth illustration of the role of B, N dopants in $Zn^{2+}$ adsorption, as shown in Figure S20. After $Zn^{2+}$ adsorption, the Zn 4s band center shifts from −5.130 eV of pure graphene to −3.717 eV of the pyrrolic-N-G-$BC_3$ configurated graphene. Compared with pure graphene, the Zn 4 s band center of pyrrolic-N-G-$BC_3$ configurated graphene is closer to the Fermi level, implying the stronger $Zn^{2+}$ adsorption ability on the surface of pyrrolic-N-G-$BC_3$ configurated graphene than that of pure graphene.[71,72] Furthermore, the charge density difference diagram of Zn-ion adsorbed pyrrolic-N-G-$BC_3$ is exhibited in Figures 6B and S21, which illustrates that the charge depletion and accumulation primarily take place on Zn and heteroatom adsorption sites. To investigate the positive effect of heteroatoms on the chemical adsorption/desorption process between C–OH and $Zn^{2+}$ ($C{-}OH + Zn^{2+} + e^- = C - O{-}Zn + H^+$), Figure 6C–E describes the reaction path diagram of $Zn^{2+}$ on the pure graphene, pyrrolic-N, and pyrrolic-N-$BC_3$ configurated graphene, respectively. As seen, Zn ions are firstly absorbed on the O site of an O−H group with a decreased total energy, and subsequently, the O−H bond forms the C−O−Zn bond, releasing free $H^+$. Notably, as the formation of the C−O−Zn bond needs to conquer a high energy barrier, it is the rate-determining step in the whole reaction process. The energy barrier that is required to be conquered for the reaction on pyrrolic-N-$BC_3$ configurated graphene is 1.913 eV, which is lower than 2.548 and 2.031 eV for pure graphene and pyrrolic-N configurated graphene, respectively, implying a stronger positive effect on the chemical adsorption of $Zn^{2+}$ on pyrrolic-N-$BC_3$ configurated graphene. The projection of the electron localization function (ELF) for pure graphene and pyrrolic-N-G-$BC_3$ configurated graphene was conducted to uncover the influence of heteroatomic motifs on the chemical adsorption capability of −OH band to $Zn^{2+}$ (Figure 6F,G). The ELF reflects the localization degree of electrons with a value between 0 and 1, where 0 represents the highest degree of electron localization (the strongest ability to form bonds), while 1 corresponds to the highest degree of electron discretization (difficult to form bonds). According to the Bader charge analysis, the C in pyrrolic-N-G-$BC_3$ presents a valence of 0.624 after the introduction of B, N atoms, which means that it loses 0.363 more electrons as compared to pure graphene with a valence of 0.261. The O atom connected to C atoms in pyrrolic-N-G-$BC_3$ gains 0.092 more electrons than that of pure graphene. That is to say, the electrons of the C atom tend to flow to N and O atoms with higher electronegativity, leading to more negative charges around N and O atoms, and relatively lower electron density concentrated on the C atom (Figure 6H). As a result, the electron-withdrawing-induced effect results in stronger polarization of O−H in the pyrrolic-N-G-$BC_3$, making it easier to break the O−H to produce $H^+$ and form C−O−Zn. Impressively, the chemical coupling-induced charge flow makes the built-in zincophilic regions become highly available and facilitates efficient ion migration, which promotes the reversible redox reaction of $Zn^{2+}$ to gain an enhanced electrochemical energy storage capability.[73]

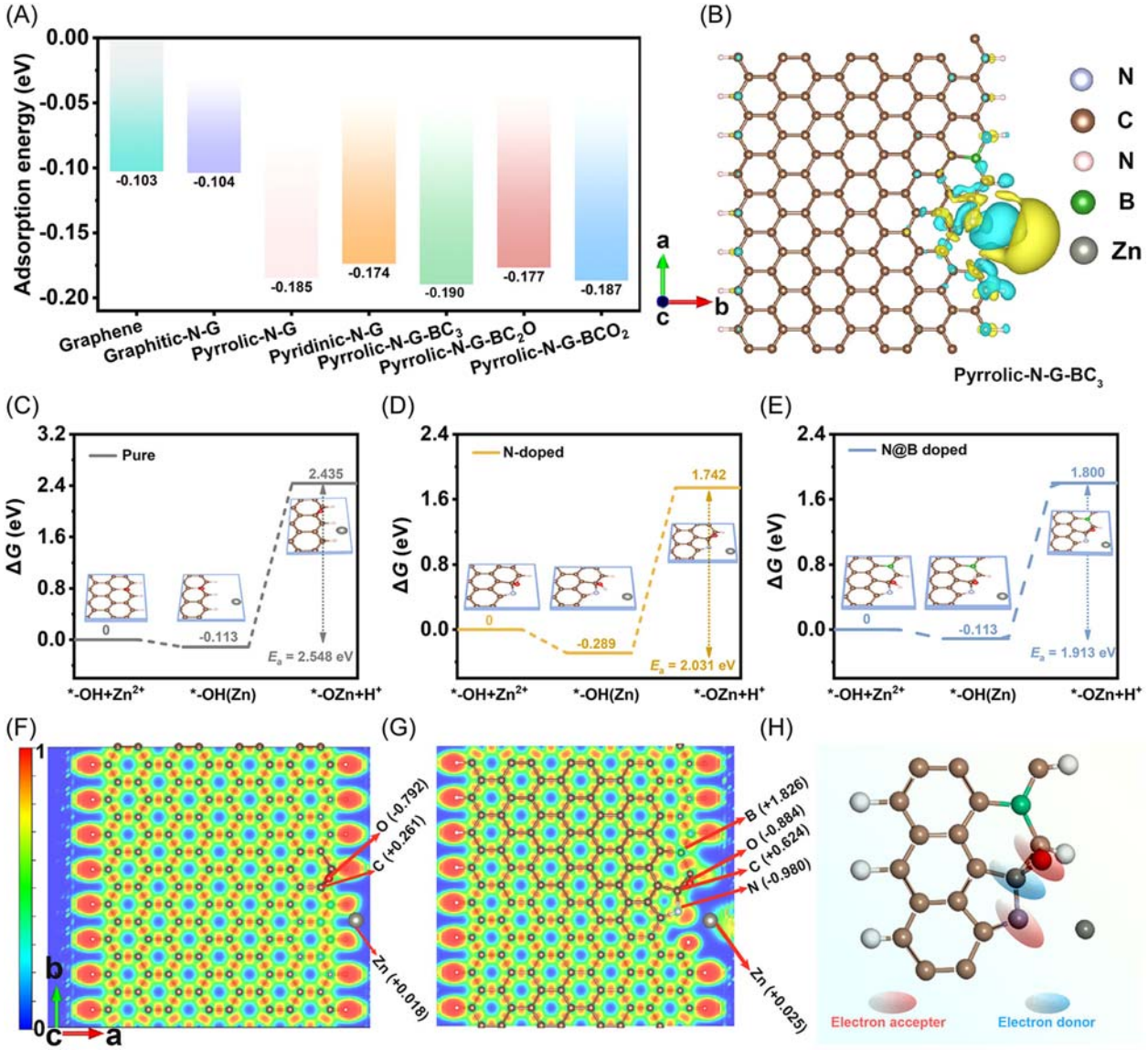


**FIGURE 6** (A) Zn ion adsorption energy of pure graphene and various heteroatom configurated graphene. (B) Charge density difference diagram of pyrrolic-N-G-$BC_3$ configuration after Zn-ion adsorption (charge accumulation and depletion are in yellow and light blue, respectively). (C–E) $\Delta G$ values of the reaction process on the pristine graphene, pyrrolic-N-G, and pyrrolic-N-G-$BC_3$ configurated graphene with −OH group, respectively. (F, G) The projection of the ELF for pure graphene and pyrrolic-N-G-$BC_3$ configurated graphene with −OH group after Zn ion adsorption. (H) Charge pattern of B-N-C-OH.

## 3 | CONCLUSION

A 3D BNPC with hierarchical porosity has been developed as a preeminent cathode for efficient Zn-ion storage. This engineered architecture exhibits integrated high-activity B/N species, well-assembled hierarchical frameworks, a relatively high surface area, and multiple pores, all of which synergistically contribute to its exceptional electrochemical performance. The BNPC cathode demonstrates an ultrahigh reversible capacity of 143.7 mAh $g^{-1}$, excellent rate performance (84.5 mAh $g^{-1}$ at 30 A $g^{-1}$), and remarkable cycle stability (a capacity retention of 98.7% after 30,000 cycles at 10 A $g^{-1}$), achieved through a mixed mechanism of electric double-layer capacitance and Faradaic redox processes. Furthermore, the as-assembled ZHC with distinctive integrated virtues of BNPC cathode affords a high-level energy of 117.15 Wh $kg^{-1}$ at a power density of 163.15 W $kg^{-1}$, even outperforming the performance of the state-of-the-art similar devices. In/ex-situ characterizations elaborately illustrate the possible reactions that occurred on the BNPC cathode. Detailed DFT calculations further elucidate the mechanism underlying the promoted Zn-ion adsorption and rapid $Zn^{2+}$ transport

facilitated by the B/N co-doping in the BNPC structure. This research not only highlights the advantages of heteroatom-doping effects in the synthesis of functional carbon materials but also provides a promising platform for the development of high-efficiency ZHCs.

## ACKNOWLEDGMENTS

The authors gratefully acknowledge the financial support by Special Projects on Regional Collaborative Innovation-SCO Science and Technology Partnership Program, International Science and Technology Cooperation Program (2022E01020), National Natural Science Foundation of China (U2003216 and 22369019), National Key Research and Development Program of China (2022YFB4101600 and 2022YFB4101601), Tianshan Talent Training Program (2023TSYCLJ0019), and Natural Science Foundation of Xinjiang Uygur Autonomous Region (2023D01C11). The authors would like to thank Shiyanjia Lab (www.shiyanjia.com) for the measurements.

## CONFLICT OF INTEREST STATEMENT

The authors declare no conflict of interest.

## ORCID

*Hongyu Mi* http://orcid.org/0000-0002-4428-5269

## REFERENCES

1. Liu M, Wu F, Feng X, et al. Molecular engineering toward sustainable development of multiple-doped hierarchical porous carbons for superior zinc ion storage. *Sci China Mater*. 2022;66(2):541-555.
2. Tang H, Yao J, Zhu Y. Recent developments and future prospects for zinc-ion hybrid capacitors: a review. *Adv Energy Mater*. 2021;11(14):2003994.
3. Liu Y, Wu L. Recent advances of cathode materials for zinc-ion hybrid capacitors. *Nano Energy*. 2023;109:108290.
4. Lu Y, Li Z, Bai Z, et al. High energy-power Zn-ion hybrid supercapacitors enabled by layered B/N co-doped carbon cathode. *Nano Energy*. 2019;66:104132.
5. Kumar R, Joanni E, Sahoo S, et al. An overview of recent progress in nanostructured carbon-based supercapacitor electrodes: from zero to bi-dimensional materials. *Carbon*. 2022;193(30):298-338.
6. Song Y, Ji K, Duan H, Shao M. Hydrogen production coupled with water and organic oxidation based on layered double hydroxides. *Exploration*. 2021;1(3):20210050.
7. Li X, Li Y, Xie S, Zhou Y, Rong J, Dong L. Zinc-based energy storage with functionalized carbon nanotube/polyaniline nanocomposite cathodes. *Chem Eng J*. 2022;427(1):131799.
8. Lou G, Pei G, Wu Y, et al. Combustion conversion of wood to N, O co-doped 2D carbon nanosheets for zinc-ion hybrid supercapacitors. *Chem Eng J*. 2021;413(1):127502.
9. Chen S, Ma L, Zhang K, Kamruzzaman M, Zhi C, Zapien JA. A flexible solid-state zinc ion hybrid supercapacitor based on co-polymer derived hollow carbon spheres. *J Mater Chem A*. 2019;7(13):7784-7790.
10. Liu Q, Zhang H, Xie J, Liu X, Lu X. Recent progress and challenges of carbon materials for Zn-ion hybrid supercapacitors. *Carbon Energy*. 2020;2(4):521-539.
11. Zhang Y, Song Z, Miao L, et al. A crystal splitting growth and self-assembly route to carbon superstructures with high energy and superstable Zn-ion storage. *Chem Eng J*. 2023;467:143497.
12. Li Y, Xiao K, Huang C, et al. Enhanced potassium-ion storage of the 3D carbon superstructure by manipulating the nitrogen-doped species and morphology. *Nano-Micro Lett*. 2020;13(1):1.
13. Li B, Yu M, Li Z, Yu C, Wang H, Li Q. Constructing flexible all-solid-state supercapacitors from 3D nanosheets active bricks via 3D manufacturing technology: a perspective review. *Adv Funct Mater*. 2022;32(29):2201166.
14. Wang Z, Zhang M, Ma W, Zhu J, Song W. Application of carbon materials in aqueous zinc ion energy storage devices. *Small*. 2021;17(19):2100219.
15. Li Z, Mi H, Bai Z, et al. Sustainable biowaste strategy to fabricate dual-doped carbon frameworks with remarkable performance for flexible solid-state supercapacitors. *J Power Sources*. 2019;418(1):112-121.
16. Li Y, Wang G, Wei T, Fan Z, Yan P. Nitrogen and sulfur co-doped porous carbon nanosheets derived from willow catkin for supercapacitors. *Nano Energy*. 2016;19:165-175.
17. Lu SY, Jin M, Zhang Y, Niu YB, Gao JC, Li CM. Chemically exfoliating biomass into a graphene-like porous active carbon with rational pore structure, good conductivity, and large surface area for high-performance supercapacitors. *Adv Energy Mater*. 2018;8(11):1702545.
18. Wang C, Yan B, Zheng J, et al. Recent progress in template-assisted synthesis of porous carbons for supercapacitors. *Adv Powder Mater*. 2022;1(2):100018.
19. Du R, Wu Y, Yang Y, et al. Porosity engineering of MOF-based materials for electrochemical energy storage. *Adv Energy Mater*. 2021;11(20):2100154.
20. Deng X, Li J, Zhu S, Ma L, Zhao N. Boosting the capacitive storage performance of MOF-derived carbon frameworks via structural modulation for supercapacitors. *Energy Stor Mater*. 2019;23:491-498.
21. Wang L, Jiao Y, Yao S, Li P, Wang R, Chen G. MOF-derived NiO/Ni architecture encapsulated into N-doped carbon nanotubes for advanced asymmetric supercapacitors. *Inorg Chem Front*. 2019;6(6):1553-1560.
22. Kshetri T, Khumujam DD, Singh TI, Lee YS, Kim NH, Lee JH. Co-MOF@MXene-carbon nanofiber-based freestanding electrodes for a flexible and wearable quasi-solid-state supercapacitor. *Chem Eng J*. 2022;437:135338.
23. Wang H, Chen Q, Xiao P, Cao L. Unlocking zinc-ion energy storage performance of onion-like carbon by promoting heteroatom doping strategy. *ACS Appl Mater Interfaces*. 2022;14(7):9013-9023.
24. Ghosh S, Barg S, Jeong SM, Ostrikov K. Heteroatom-doped and oxygen-functionalized nanocarbons for high-performance supercapacitors. *Adv Energy Mater*. 2020;10(32):2001239.
25. Li J, Zhang J, Yu L, et al. Dual-doped carbon hollow nanospheres achieve boosted pseudocapacitive energy storage for aqueous zinc ion hybrid capacitors. *Energy Stor Mater*. 2021;42:705-714.

26. Song Z, Miao L, Ruhlmann L, et al. Self-assembled carbon superstructures achieving ultra-stable and fast proton-coupled charge storage kinetics. *Adv Mater*. 2021;33(49):2104148.
27. Yang M, Bai Q. Flower-like hierarchical Ni-Zn MOF microspheres: efficient adsorbents for dye removal. *Colloids Surf A*. 2019;582:123795.
28. Arul P, John SA. Organic solvent free in situ growth of flower like Co-ZIF microstructures on nickel foam for glucose sensing and supercapacitor applications. *Electrochim Acta*. 2019;306:254-263.
29. Li M, Tang M, Xue P, Dai H, He T, Wang Z. A binder-free, well-integrated metal-organic frameworks@polypyrrole nanofilm electrocatalyst for highly efficient and selective reduction of carbon dioxide. *Mater Today Energy*. 2022;30:101140.
30. Qin Z, Xu Y, Liu L, et al. Ni-MOF composite polypyrrole applied to supercapacitor energy storage. *RSC Adv*. 2022;12(45):29177-29186.
31. Majidi R, Farhadi A, Danaee I, Panah NB, Zarei D, Nikmanesh S. Investigation of synthesized planar Cu-MOF and spherical Ni-MOF nanofillers for improving the anti-corrosion performance of epoxy coatings. *Prog Org Coat*. 2023;183:107803.
32. Jafarinejad-Farsangi S, Ansari-Asl Z, Rostamzadeh F, Neisi Z. Polypyrrole/Ni (II) metal-organic frameworks nanocomposites: fabrication, characterization, and biocompatibility investigations. *Mater Today Commun*. 2021;28:102559.
33. Cai W, Chen J, Liu L, Yang Y, Wang H. Tuning the structural stability of $LiBH_4$ through boron-based compounds towards superior dehydrogenation. *J Mater Chem A*. 2018;6(3):1171-1180.
34. Yao Y, Huang G, Liu Y, et al. Facile synthesis of B/N co-doped porous carbon nanosheets with high heteroatom content and electrical conductivity for excellent-performance supercapacitors. *Appl Surf Sci*. 2022;580:152236.
35. Wang Y, Yang J, Liu S, et al. 3D graphene-like oxygen and sulfur-doped porous carbon nanosheets with multilevel ion channels for high-performance aqueous Zn-ion storage. *Carbon*. 2023;201:624-632.
36. Chen X, Ye P, Wang H, Huang H, Zhong Y, Hu Y. Discriminating active B-N sites in coralloidal B, N dual-doped carbon nano-bundles for boosted zn-ion storage capability. *Adv Funct Mater*. 2023;33(12):2212915.
37. Yuan M, Wang Z, Rao Y, et al. Laser direct writing O/N/S Co-doped hierarchically porous graphene on carboxymethyl chitosan/lignin-reinforced wood for boosted microsupercapacitor. *Carbon*. 2023;202:296-304.
38. Xu J, Li Z, Sun P, et al. Effective incorporation of nitrogen and boron in worm-like carbon foam for confining polysulfides. *Carbon*. 2019;155:379-385.
39. Wang B, Gu L, Yuan F, et al. Edge-enrich N-doped graphitic carbon: boosting rate capability and cyclability for potassium ion battery. *Chem Eng J*. 2022;432:134321.
40. Leng C, Fedoseeva YV, Zhao Z, et al. Rational-design heteroatom-doped cathode and ion modulation layer modified Zn anode for ultrafast zinc-ion hybrid capacitors with simultaneous high power and energy densities. *J Power Sources*. 2022;536:231484.
41. Yang L, Cao Z, Chen D, et al. Boron enriched edge-nitrogen defective carbon network toward high-capacity capacitive deionization. *Chem Eng J*. 2024;489:151214.
42. Zhang Z, Ouyang D, Chen D, Yang L, Zhu H, Yin J. Tuning nitrogen species in 3D porous carbon via boron doping for boosted Zn-ion storage capability. *J Mater Chem A*. 2024;12(5):3026-3033.
43. Dahal B, Mukhiya T, Ojha GP, et al. In-built fabrication of MOF assimilated B/N co-doped 3D porous carbon nanofiber network as a binder-free electrode for supercapacitors. *Electrochim Acta*. 2019;301:209-219.
44. Wang X, Sun G, Routh P, Kim DH, Huang W, Chen P. Heteroatom-doped graphene materials: syntheses, properties and applications. *Chem Soc Rev*. 2014;43(20):7067-7098.
45. Zhu T, Li S, Ren B, Zhang L, Dong L, Tan L. Plasma-induced synthesis of boron and nitrogen co-doped reduced graphene oxide for super-capacitors. *J Mater Sci*. 2019;54(13):9632-9642.
46. Cançado LG, Jorio A, Ferreira EHM, et al. Quantifying defects in graphene via Raman spectroscopy at different excitation energies. *Nano Lett*. 2011;11(8):3190-3196.
47. Liu C, Chang X, Mi H, Guo F, Ji C, Qiu J. Modulating pore nanostructure coupled with N/O doping towards competitive coal tar pitch-based carbon cathode for aqueous Zn-ion storage. *Carbon*. 2024;216:118523.
48. Zhang X, Jiang C, Li H, et al. Rational design of activated graphitic carbon spheres with optimized ion and electron transfer channels for zinc-ion hybrid capacitors. *J Colloid Interface Sci*. 2023;651:211-220.
49. Chen X, Ye P, Wang H, Huang H, Zhong Y, Hu Y. Discriminating active B N sites in coralloidal B, N dual-doped carbon nano-bundles for boosted Zn-ion storage capability. *Adv Funct Mater*. 2023;33(12):2212915.
50. Xu H, He W, Li Z, et al. Revisiting charge storage mechanism of reduced graphene oxide in zinc ion hybrid capacitor beyond the contribution of oxygen-containing groups. *Adv Funct Mater*. 2022;32(16):2111131.
51. Gao Y, Li G, Wang F, et al. A high-performance aqueous rechargeable zinc battery based on organic cathode integrating quinone and pyrazine. *Energy Storage Mater*. 2021;40:31-40.
52. Zhang H, Chen Z, Zhang Y, et al. Boosting Zn-ion adsorption in cross-linked N/P co-incorporated porous carbon nanosheets for the zinc-ion hybrid capacitor. *J Mater Chem A*. 2021;9(30):16565-16574.
53. Deng X, Li J, Shan Z, Sha J, Ma L, Zhao N. A N, O co-doped hierarchical carbon cathode for high-performance Zn-ion hybrid supercapacitors with enhanced pseudocapacitance. *J Mater Chem A*. 2020;8(23):11617-11625.
54. Liu P, Gao Y, Tan Y, et al. Rational design of nitrogen doped hierarchical porous carbon for optimized zinc-ion hybrid supercapacitors. *Nano Res*. 2019;12(11):2835-2841.
55. Ali A, Shen PK. Nonprecious metal's graphene-supported electrocatalysts for hydrogen evolution reaction: fundamentals to applications. *Carbon Energy*. 2020;2(1):99-121.
56. Chang X, Zhu Q, Zhao Q, et al. 3D porous $Co_3O_4$/MXene foam fabricated via a sulfur template strategy for enhanced Li/K-ion storage. *ACS Appl Mater Interfaces*. 2023;15(6):7999-8009.
57. Lu Y, Liang J, Deng S, et al. Hypercrosslinked polymers enabled micropore-dominant N,S Co-doped porous carbon for ultrafast electron/ion transport supercapacitors. *Nano Energy*. 2019;65:103993.
58. Javed MS, Najam T, Hussain I, et al Fundamentals and scientific challenges in structural design of cathode materials for

zinc-ion hybrid supercapacitors. *Adv Energy Mater*. 2022;13(3):2202303.
59. Yang Q, Huang Z, Li X, et al. A wholly degradable, rechargeable Zn-$Ti_3C_2$ MXene capacitor with superior anti-self-discharge function. *ACS Nano*. 2019;13(7):8275-8283.
60. García-Cruz L, Ratajczak P, Iniesta J, Montiel V, Béguin F. Self-discharge of AC/AC electrochemical capacitors in salt aqueous electrolyte. *Electrochim Acta*. 2016;202:66-72.
61. Jiang Y, Ba D, Li Y, Liu J. Noninterference revealing of "layered to layered" zinc storage mechanism of δ-$MnO_2$ toward neutral Zn–Mn batteries with superior performance. *Adv Sci*. 2020;7(6):1902795.
62. Yoo HD, Han SD, Bayliss RD, et al. Rocking-chair"-type metal hybrid supercapacitors. *ACS Appl Mater Interfaces*. 2016;8(45):30853-30862.
63. Li Y, Yang W, Yang W, et al. Towards high-energy and anti-self-discharge Zn-Ion hybrid supercapacitors with new understanding of the electrochemistry. *Nano-Micro Lett*. 2021;13(1):95.
64. El-Kady MF, Kaner RB. Scalable fabrication of high-power graphene micro-supercapacitors for flexible and on-chip energy storage. *Nat Commun*. 2013;4(1):1475.
65. Yang Z, Chang X, Mi H, et al. Oxygen-enriched pitch-derived hierarchically porous carbon toward boosted zinc-ion storage performance. *J Colloid Interface Sci*. 2024;658:506-517.
66. Li X, Li Y, Zhao X, Kang F, Dong L. Elucidating the charge storage mechanism of high-performance vertical graphene cathodes for zinc-ion hybrid supercapacitors. *Energy Storage Mater*. 2022;53:505-513.
67. Yuan R, Wang H, Shang L, et al. Revealing the self-doping defects in carbon materials for the compact capacitive energy storage of Zn-Ion capacitors. *ACS Appl Mater Interfaces*. 2023;15(2):3006-3016.
68. Wang L, Peng M, Chen J, Hu T, Yuan K, Chen Y. Eliminating the micropore confinement effect of carbonaceous electrodes for promoting Zn-Ion storage capability. *Adv Mater*. 2022;34(39):2203744.
69. Peng Z, Bannov AG, Li S, et al. Coupling uniform pore size and multi-chemisorption sites: hierarchically ordered porous carbon for ultra-fast and large zinc ion storage. *Adv Funct Mater*. 2023;33(40):2303205.
70. Li Z, Chen D, An Y, et al. Flexible and anti-freezing quasi-solid-state zinc ion hybrid supercapacitors based on pencil shavings derived porous carbon. *Energy Storage Mater*. 2020;28:307-314.
71. Yang J, Cao Y, Zhang S, et al. Interstitial hydrogen atom to boost intrinsic catalytic activity of tungsten oxide for hydrogen evolution reaction. *Small*. 2023;19(29):2207295.
72. Sun Y, Ding S, Xia B, Duan J, Antonietti M, Chen S. Biomimetic FeMo (Se, Te) as joint electron pool promoting nitrogen electrofixation. *Angew Chem Int Ed*. 2022;61(16):e202115198.
73. Song Z, Miao L, Ruhlmann L, et al. Lewis pair interaction self-assembly of carbon superstructures harvesting high-energy and ultralong-life zinc-ion storage. *Adv Funct Mater*. 2022;32(48):2208049.

## SUPPORTING INFORMATION

Additional supporting information can be found online in the Supporting Information section at the end of this article.

**How to cite this article:** Jin C, Guo F, Mi H, et al. Template-oriented synthesis of boron/nitrogen-rich carbon nanoflake superstructure for high-performance Zn-ion hybrid capacitors. *Carbon Energy*. 2025;7:e673. doi:10.1002/cey2.673